## ARTICLE   OPEN

Check for updates

# Deep learning for exploring ultra-thin ferroelectrics with highly improved sensitivity of piezoresponse force microscopy

Panithan Sriboriboon [1], Huimin Qiao[1,2], Owoong Kwon[1,2], Rama K. Vasudevan [3], Stephen Jesse[3] and Yunseok Kim [1,2✉]

Hafnium oxide-based ferroelectrics have been extensively studied because of their existing ferroelectricity, even in ultra-thin film form. However, studying the weak response from ultra-thin film requires improved measurement sensitivity. In general, resonance-enhanced piezoresponse force microscopy (PFM) has been used to characterize ferroelectricity by fitting a simple harmonic oscillation model with the resonance spectrum. However, an iterative approach, such as traditional least squares (LS) fitting, is sensitive to noise and can result in the misunderstanding of weak responses. In this study, we developed the deep neural network (DNN) hybrid with deep denoising autoencoder (DDA) and principal component analysis (PCA) to extract resonance information. The DDA/PCA-DNN improves the PFM sensitivity down to 0.3 pm, allowing measurement of weak piezoresponse with low excitation voltage in 10-nm-thick $Hf_{0.5}Zr_{0.5}O_2$ thin films. Our hybrid approaches could provide more chances to explore the low piezoresponse of the ultra-thin ferroelectrics and could be applied to other microscopic techniques.

## INTRODUCTION

Ferroelectric materials are of great interest because of their intriguing physical properties, such as their bi-stable polarization states and fast switching speed. Since reporting fluorite ferro-electrics in 2011[1], extensive studies have been performed for exploring and improving the ferroelectricity of these materials[2–5], for example, $HfO_2$, $Hf_{0.8}Zr_{0.2}O_2$, Al: $HfO_2$, and $ZrO_2$, because of their existing ferroelectricity, even in less than 10 nm thin films.

While piezoresponse force microscopy (PFM) has been widely used to evaluate ferroelectricity at the nanoscale[6], a conventional PFM, which is operated at a single off-resonance frequency, can be of limited use when evaluating ferroelectricity in ultra-thin ferroelectrics, including fluorite ferroelectrics, because of the insufficient sensitivity of conventional PFM techniques[3]. Accordingly, resonance-enhanced PFM techniques, such as band-excitation (BE) and dual AC resonance tracking, have been utilized for the evaluation of ultra-thin ferroelectrics[7–10] because the resonance of cantilevers allows one to amplify the sensitivity and increase the signal-to-noise ratio (SNR) by the quality factor of the resonance peak. To extract the resonance information of BE-PFM (such as amplitude, phase, and resonance frequency), the spectrum obtained around the resonance frequency is analyzed by fitting the measured data based on a simple harmonic oscillator (SHO) model[11] with a traditional least-squares (LS) method.

Nevertheless, if the piezoresponse is weak because of the ultra-thin material, it can be difficult to accurately analyze the resonance because of a low SNR. Thus, improving PFM sensitivity for exploring more complex ferroelectric behavior and properly evaluating the ferroelectricity of ultra-thin ferroelectrics is still required. In fact, an improvement in PFM sensitivity was reported based on the application of deep learning algorithms[12] by improving the priors that are then fed into the LS method. However, this deep learning method still requires the LS method, which in turn strongly depends on the initial guesses. If the deep learning algorithms fail to provide a suitable prior for the LS

method, as can be the case in low SNR measurements of weak piezoresponse materials[13,14] or in challenging noisy environments[15,16], the fitting results can still be poor, eventually causing a misinterpretation[12]. Furthermore, in cases of working with large datasets, an iterative approach of the LS method is time-consuming. Up to now, the rapid fitting method capable of handling noise has remained challenging for extracting of resonance information. Therefore, it is important to explore an accurate and efficient approach to address the functional fitting issue.

In this study, we demonstrate highly improved PFM sensitivity based on a deep neural network (DNN) that combines denoising elements without the need for further optimization by the LS method. The deep denoising autoencoder (DDA) and principal component analysis (PCA) were assigned for the noise reduction task, and then the DNN was applied to the denoised dataset. These noise-reducing elements directly address noisy outliers to improve the SNR, resulting in increased PFM sensitivity. These implemented workflows for BE-PFM were validated using ferroelectric model samples of periodically poled lithium niobate (PPLN) and 10 nm-thick $Hf_{0.5}Zr_{0.5}O_2$ (HZO) thin films. Compared to the traditional LS method and a previously reported DNN-LS method, the proposed workflows of DDA-DNN and PCA-DNN remarkably improved the SNR and PFM sensitivity. In particular, the results for HZO thin films presented the feasibility of exploring very weak piezoresponse. The PCA-DNN approach successfully extracts the low piezoresponse, allowing switching events of the HZO thin films to be observed using a low excitation voltage. Furthermore, our approach reduces the time necessary for the evaluation of resonance information because, while the LS method is time-consuming for working with large amounts of data, the DNN method is known as a relatively fast one that can be parallelized across GPUs with outputs given in ms time[12]. Thus, the application of fully machine learning algorithms without the LS method can provide a faster and more accurate resonance analysis, and especially important when fast feedback is required

[1]School of Advanced Materials and Engineering, Sungkyunkwan University (SKKU), Suwon, Republic of Korea. [2]Research Center for Advanced Materials Technology, Core Research Institute, Suwon, Republic of Korea. [3]Center for Nanophase Materials Sciences, Oak Ridge National Laboratory, Oak Ridge, TN, USA. ✉email: yunseokkim@skku.edu
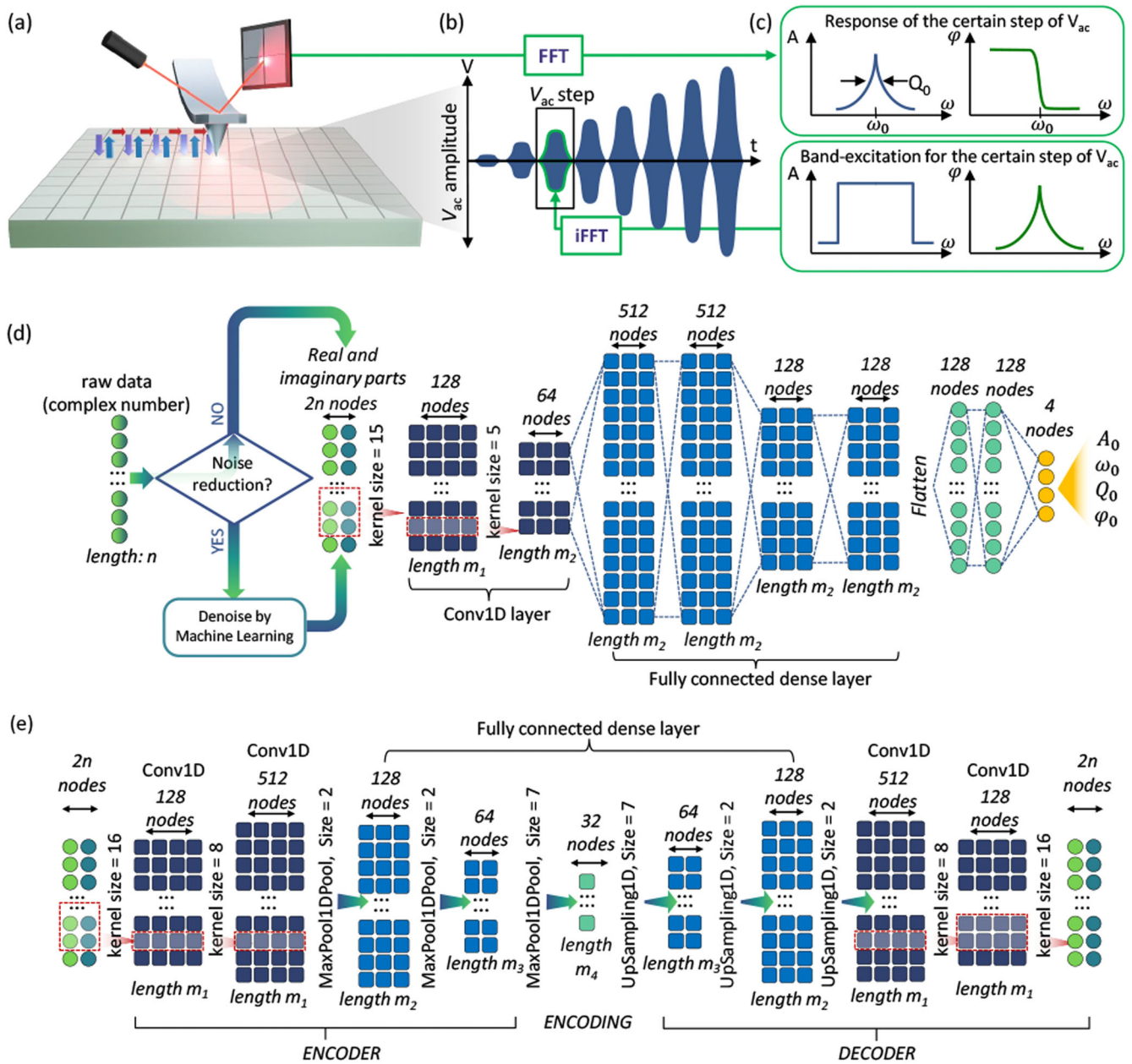
**Fig. 1 Scheme of the PFM measurements integrated with deep learning. a** PFM spectroscopy measurement where the resonance spectrum records pixel-by-pixel while the probe moves according to the mapping positions. **b** The waveform for the $V_{ac}$ amplitude sweep consists of the BE waves with a predefined frequency range across the contact resonance frequency and different $V_{ac}$ amplitudes ($V_{ac}$ steps). During the measurement, the cantilever oscillation induced by the waveform is acquired at every pixel as the PFM dataset. After the FFT, the piezoresponse oscillation spectrum of a complex value can be converted into (**c**) amplitude and phase as a function of frequency, and every single datum in the dataset can be indexed by the row, column, $V_{ac}$ step, and frequency bin. **d** Schematic of the DNN workflow with the noise reduction element. **e** Schematic of the noise reduction element of the DDA, the component of encoder, encoding, and decoder layers, in which the type and dimensionality are specified on the top of the layer. The DNN and DDA input data are a stacked $2 \times N$ matrix of the real and imaginary parts of the piezoresponse signal.

to the instrument to enable automated and autonomous experiments.

## RESULT AND DISCUSSION

### Deep learning for PFM signal extraction

One of the well-known resonance-enhanced PFM techniques is BE-PFM of which spectroscopy is presented in Fig. 1a. The BE waveform is configured in the time domain and applied to the tip to excite the tip-sample interaction, which results in the cantilever

deflection captured in the frequency domain through the fast Fourier transform (FFT) (see Fig. 1b, c). The FFT output gives a complex value that is generally represented by amplitude and phase as a function of frequency. The resonance information from the FFT output can be analyzed by fitting the measured data based on the SHO model as follows[11]:

$$f(\omega) = \frac{A\omega_r^2 e^{i\varphi}}{\omega^2 - \frac{i\omega\omega_r}{Q} - \omega_r^2}, \qquad (1)$$

where amplitude $A$, phase $\varphi$, resonance frequency $\omega_r$, and quality factor $Q$ are the four major SHO parameters[11]. The obtained amplitude and phase correspond to the magnitude of piezo-response and direction of polarization state.

Thus, the SHO functional fitting of the BE-PFM is the key to extracting the physical properties of the systems being analyzed. The traditional method for SHO functional fitting is the LS method, which presents a challenge when determining the initial guess values ($A_0$, $\omega_0$, $Q_0$, and $\varphi_0$) of the four major SHO parameters ($A$, $\omega$, $Q$, and $\varphi$); this is because giving good initial guessing parameters becomes particularly difficult with a large number of fitting parameters involved in LS fitting[17]. Furthermore, the SHO functional fitting becomes more complicated in cases with unavoidable noise from the experimental setup. In the present case, either a low $V_{ac}$ or weak piezoresponse could lead to a low SNR. A drawback of the traditional LS fitting can be examined by a $V_{ac}$ amplitude sweep waveform (see Fig. 1b). Ideally, the piezo-response increases proportionally with $V_{ac}$ amplitude at a rate of effective piezoelectric coefficient of the sample[18–20], while the noise is independent of $V_{ac}$. In fact, the LS fitting is sensitive to outliers, which have a large influence on the fit because squaring the residuals amplifies the effects of these extreme data points. Accordingly, the algorithms are likely to become trapped by these outliers, which is one of many inappropriate local minima instead of the global minima. We note that, although the use of a high $V_{ac}$ could be a practical way to obtain a high SNR, the high $V_{ac}$ amplitude could lead to a nonlinear response or sample degradation[21]; thus, it is an undesirable way to address the issue.

Alternatively, deep learning shows great promise in overcoming the limitations and challenges of the traditional LS fitting mentioned above. For instance, an approach using a DNN, which is well-known for feature recognition[12,22–24], was proven to be effective at predicting the SHO parameters at low SNR[12]. However, the DNN lacks an optimization process to minimize the error between the predicted data and noisy raw data. Meanwhile, another method[12] uses a hybrid of DNN and LS approaches (henceforth referred to as DNN-LS), where the DNN predicts initial estimate parameters and the LS optimizes SHO function parameters. Although this approach is interesting, it suffers from the noisy SHO with data outliers (see Supplementary Fig. 1). Specifically, the data outliers in the SHO spectrum may produce a peak-like SHO characteristic, leading to poor fitting or even misinterpreting DNN-LS results[12]. In addition, even though the DNN rapidly predicts the SHO parameters, combining the LS with the DNN result can be time-consuming. Therefore, it is still necessary to explore an effective, efficient, and accurate approach for the extraction of SHO parameters.

Considering the main obstacle of SHO fitting at low SNR is the misinterpretation because of the noisy outlier, resulting in a poor PFM sensitivity. Because directly handling the noise could be an effective solution, we propose a hybrid workflow associated with DNN for SHO parameter prediction. As shown in Fig. 1d, the idea is to use machine learning to reduce noise, especially the data outliers, prior to the DNN prediction. To directly manage the noise, we train the DDA, which is a well-known and practical machine learning technique, to map noisy data to low-noise data[25,26], as shown in Fig. 1e. Then, we train the DNN to predict the four major SHO parameters from the input data vector (see the details in Supplementary Note 1). We henceforth call this hybrid model as the DDA-DNN.

To train the DDA-DNN model, we employed the batch generator method[12] to combat overfitting. The batch generator created a new batch of noisy data with 64,000 SHO spectra of four random major SHO parameters, which were split into 51,200 for training and 12,800 for validation, and passed through the network only once. This procedure was repeated 50 times during the training. For the trained DNN used in this hybrid workflow, the validation accuracy was 0.75 with a validation loss of 0.015. For the

training, the DDA model was trained to reconstruct the low-noise SHO dataset from the noisy SHO dataset using the batch generator method. The training condition of DDA using the batch generator method was almost the same as DNN, except that the DDA was trained to reconstruct the no-noise spectrum from the noisy spectrum. After training, the average validation loss of the DDA was 0.0003.

## Improved signal extraction by denoising

To illustrate denoising using DDA, we simulated the noisy dataset by varying the amplitude of the SHO function with a constant noise level, as shown in Fig. 2a, b. The SNR of the simulated dataset was defined by the maximum amplitude ($A_{max}$) of the simulated signal divided by the standard deviation of the noise ($\sigma_{noise}$). We applied DDA to the simulated noisy dataset of Fig. 2a, b, which resulted in the low-noise dataset shown in Fig. 2c, d, respectively. It is obvious that the quality of the reconstructed data of DDA was relative to the SNR. Accordingly, we further evaluated the reconstruction loss of DDA as a function of SNR, as shown in Supplementary Fig. 3. The DDA works well for denoising at high SNR, as shown in Fig. 2c, d. Nevertheless, although DDA denoising was expected to improve the DNN prediction, the DDA reconstructed a defective spectrum at SNR less than 3 (individual spectrum not shown here). This might be because the DDA was not trained to recognize the interdependency features of the input datasets.

To take advantage of the interdependency between the dataset components for further improvement of noise reduction, we switched to PCA, which is an alternative denoising method. This well-known technique is used to simplify and visualize the complexity of multidimensional data while retaining trends and patterns[27–29]. The basis of PCA noise reduction is that a well-behaved signal should have more variance and therefore belong to the first few components, as opposed to the more scattered noise. Thus, the reconstruction with the first few PCA components will deliver a greatly noise-reduced dataset. Therefore, the reconstruction of data with only high variance principal components (PCs) can exclude the noise-effected PCs, that is, the redundant dimension of noise. In the actual measurement dataset, this selected dimension of the sub-dataset generally retains the SHO features of resonance frequency and quality factor. The input dataset was projected into 56 PCs by PCA, and the low-noise dataset (Fig. 2e, f) were constructed using 1 PC. This 1 PC corresponds to a 25% explained variant of the dataset (see Supplementary Figs. 2–4 for further discussion). The number of reconstructed PCs (1–56) can be varied to optimize the reconstruction loss of the noise reduction, as shown in Supplementary Fig. 3.

To explore the effect of the denoising process on the SHO parameter extraction accuracy, we compared the final results of fitting and prediction using LS, DNN-LS, DDA-DNN, and PCA-DNN on the simulated dataset. The simulated dataset was generated based on the SHO function as described earlier in Eq. 1 with random parameters of quality factor and resonance frequency. Figure 2g displays dimensional indexing, that is, columns, rows, and points, of the simulated dataset. One of many planes in the points-rows plane was extracted from the simulated dataset to depict the phase contrast corresponding to the rows, as shown in Fig. 2h. The amplitude parameter increases along the point axis with a constant noise level, as depicted in Fig. 2i, indicating that the SNR increases along the point axis. We note that the phase contrast between the upward and downward domains of this simulated dataset must be $\pi$ for the ideal SHO parameter extraction. The optimization guesses with LS fitting on the simulated dataset (Fig. 2l) presented a good phase contrast when the SNR was high. However, when the SNR was lower than 8, the phase contrast (Fig. 2j) and deviation (Fig. 2k) gradually worsened.
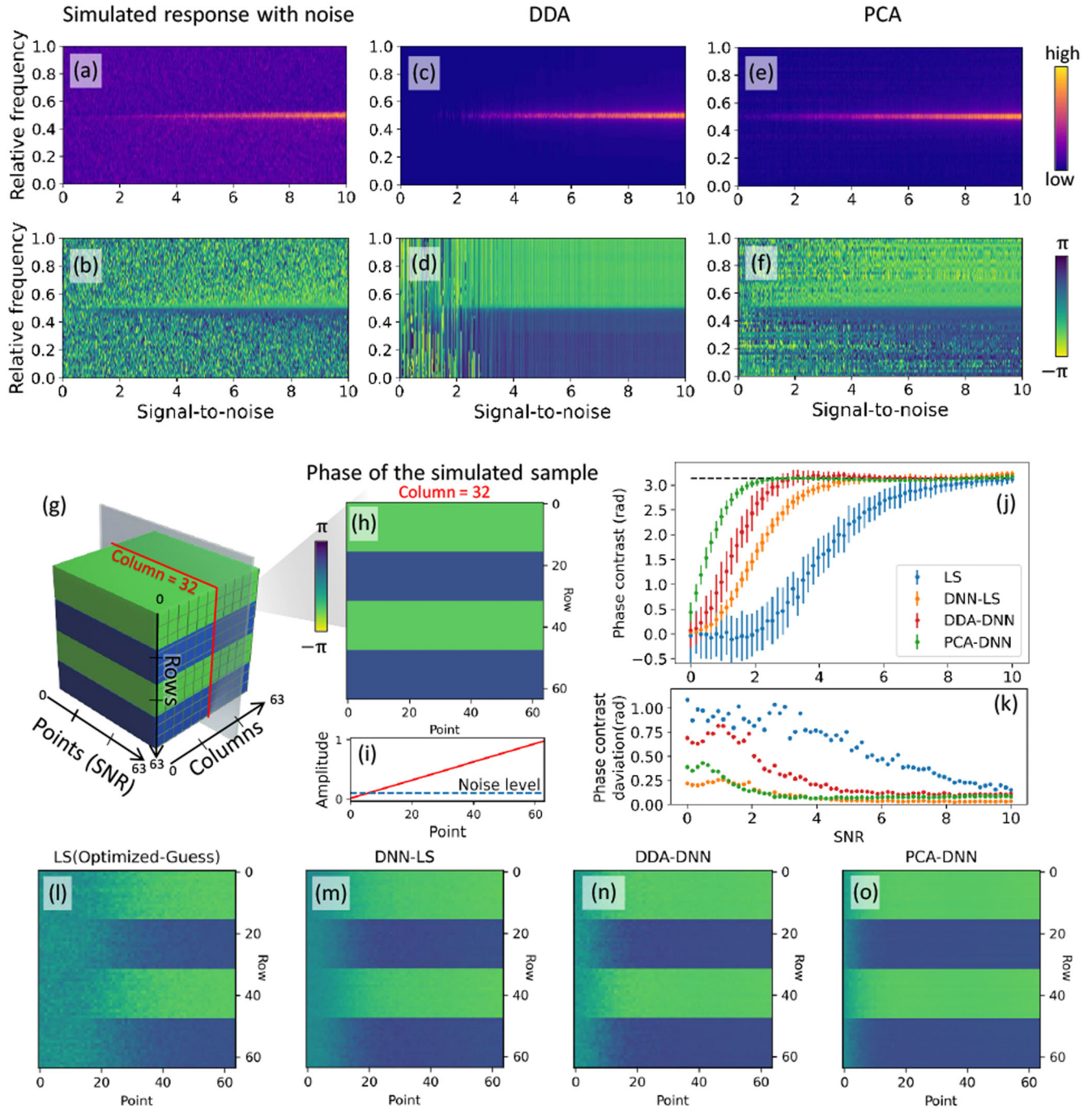
Fig. 2 **Noise reduction and phase contrast evaluation of the simulated piezoelectric domains.** a–f Noise reduction of the simulated SHO dataset using DDA and PCA: (a, c, e) amplitude and (b, d, f) phase as a function of SNR. a, b Simulated SHO data with a constant noise level, quality factor, phase, and reducing amplitude in the SNR axis, and (c–f) denoised data using DDA and PCA, respectively. g Visualization of the simulated signal for phase contrast evaluation, in which the phase parameter of the response is specified as two values of $-\pi/2$ and $\pi/2$, equivalent to the positive and negative polarization orientation, respectively. h The points-rows plan shows the phase of the simulated signal extracted from (g) at column number 32. i Amplitude variant with a constant noise level along the point axis. We note that the point and SNR are equivalent axes. j Phase contrast and (k) corresponding deviation were extracted from the SHO fitting and prediction results of (l) LS with the optimized initial guess method, (m) DNN-LS, (n) DDA-DNN, and (o) PCA-DNN. The phase contrast is calculated by the difference between the average values of two phases, that is, the phase represented by blue and green in (h).

The DNN-LS approach (Fig. 2m) displayed a better phase contrast and deviation compared to the optimization guess LS fitting method when the SNR was higher than 5 (Fig. 2j, k). For the DDA-DNN method (Fig. 2n), when the SNR was higher than 3, the phase contrast was closer to the ideal case (black dashed line, (Fig. 2j)). However, the deviation of DDA-DNN was larger at a low SNR compared to that of DNN-LS (Fig. 2k). The PCA-DNN (Fig. 2j, k, o) validates the usefulness of PCA, as shown by the better prediction of SHO parameters regarding the phase contrast, phase contrast deviation, and SNR limitation, especially at low SNR. We note that, when the SNR drops below 1, it is hard to distinguish between the PFM signal and noise. The details for DDA/PCA-DNN can be found
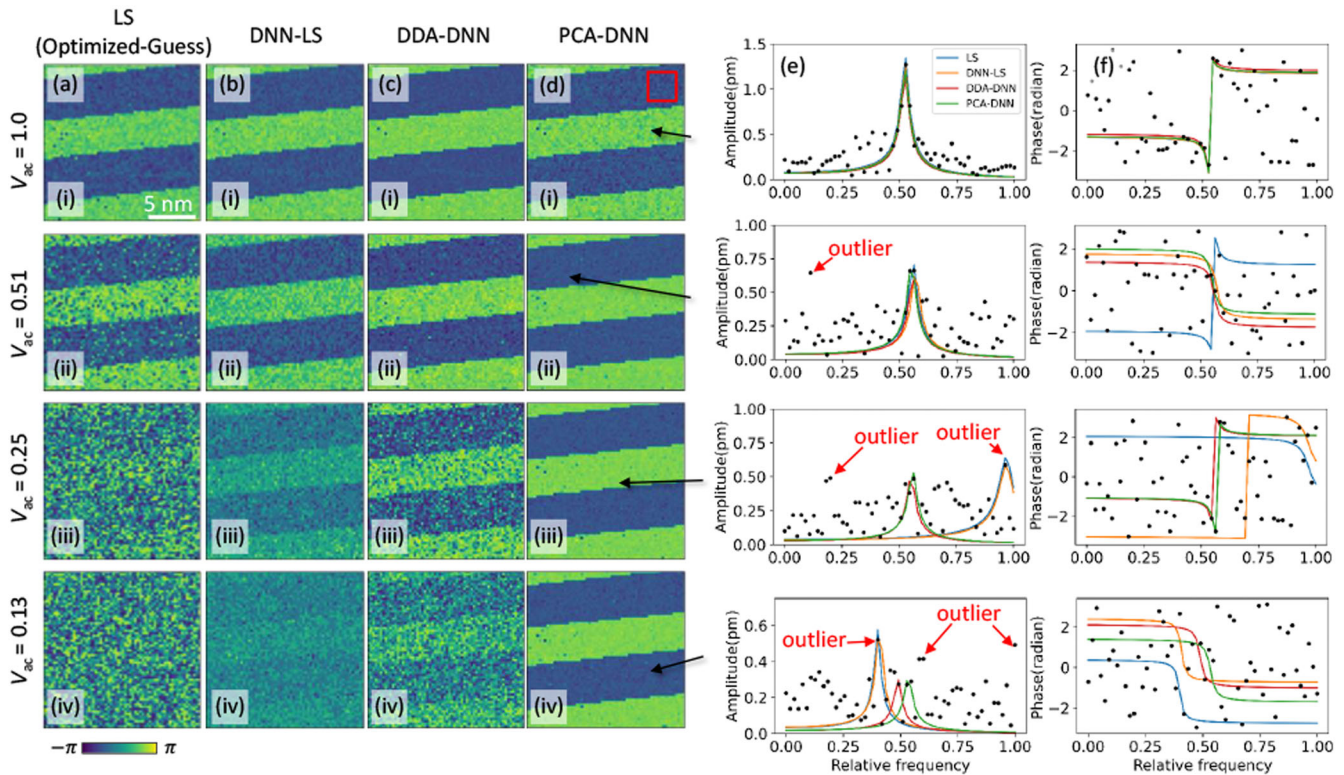
**Fig. 3 Comparison of the fitted and predicted SHO phase images for the actual dataset of PPLN.** The dataset was acquired using the $V_{ac}$ amplitude sweep measurement with maximum $V_{ac} = 1$ V: phase images of (**a**) optimized LS, (**b**) DNN-LS, (**c**) DDA-DNN, and (**d**) PCA-DNN at different $V_{ac}$ steps of (i) 1.0 $V_{ac}$, (ii) 0.51 $V_{ac}$, (iii) 0.25 $V_{ac}$, and (iv) 0.13 $V_{ac}$, respectively. **e, f** Raw data points and corresponding fitted and predicted lines of different methods for (**e**) amplitude and (**f**) phase. The black and red arrows in (**d, e**) are the exact pixels of the raw data and the data outlier that could induce poor fitting of the LS and DNN-LS, respectively. We note that the PCA-DNN was denoised using 1 PC.

in Supplementary Fig. 8. We also note that, because LS is time-consuming (see Supplementary Table 1), we could replace it in the denoising process with DDA or PCA for DNN because the phase contrast and deviation of DDA-DNN-LS (or PCA-DNN-LS) were nearly identical to those of DDA-DNN (or PCA-DNN) (see Supplementary Figs. 5–7). Thus, the application of fully machine learning algorithms without the LS method can be effective.

## Comparison of fitting workflows for PFM images

To compare the SHO fitting and prediction of LS, DNN-LS, DDA-DNN, and PCA-DNN on the real experimental dataset, we examined these four methods on the PFM images of the PPLN dataset at different $V_{ac}$ steps. In such a case, the $V_{ac}$ amplitude determines the SNR. As shown in Fig. 3ai–di, the fitted PFM phase images at the high $V_{ac}$ of 1.0 $V_{ac}$, that is, at high SNR, exhibited a relatively clear phase contrast for all four fitting methods. As expected, all four methods gave good fitting and prediction results, as shown in Fig. 3e, f. When the SNR decreased slightly, as represented by a step of 0.51 $V_{ac}$, the "poor-fit" pixel of the phase image became more noticeable in the LS method compared to that in the hybrid methods. The poor-fit pixel in Fig. 3aii corresponds to the substandard guessing parameters of the LS fitting method, which can easily be improved using DNN-LS, as shown in Fig. 3bii. Nevertheless, when the SNR drops further, the DNN-LS method is no longer able to notably improve the fitting results, as demonstrated in Fig. 3aiii, aiv, biii, biv for LS and DNN-LS respectively. We considered that the limitation of the DNN-LS fitting method resides in the noise corresponding to the data outliers that act like a trap for LS and DNN-LS, as shown in the fitting spectra in Fig. 3eiii, fiii, respectively. Therefore, after implementing the DDA and PCA to reduce the data outlier from

the SHO spectrum, the DNN was applied for the SHO parameter prediction. Consequently, the improved SHO parameter extraction improves the phase contrast of PFM images, as shown in Fig. 3ciii, civ for DDA-DNN and Fig. 3diii, div for PCA-DNN, respectively. Accordingly, the predicted spectra of DDA-DNN and PCA-DNN were not trapped by the data outliers, as shown in Fig. 3eiii, eiv, fiii, fiv (see more details in Supplementary Fig. 9). On the other hand, at 0.25 and 0.13 $V_{ac}$, the prediction results of the PCA-DNN gave a better phase contrast relative to the DDA-DNN (see Fig. 3ciii, civ, diii, div). Nevertheless, we believe that the performance of DDA can be further improved by better architectural design and development. Despite this, because we focused on the proof-of-concept using the DDA-DNN workflow for the SHO parameter extraction, advanced DDN and the DNN architecture will be the focus of a future study.

## Quantification of PFM sensitivity

It is worth quantifying both sensitivity and SNR relative to the workflow. Prior to the exploration of these values, the noise level was first explored from the PFM amplitude of the PPLN dataset in Fig. 4. Figure 4a, b are two-dimensional histogram plots of the as-acquired spectrum of the PPLN dataset. In Fig. 4a, the area of a high-density signal with a low amplitude value indicates a constant signal that does not change relative to the increasing $V_{ac}$. In particular, at $V_{ac} \approx 0$, where there is ideally no PFM amplitude, the signal density does not change as well. Therefore, this area can be regarded as a steady noise, i.e., the instrumental background noise. By the Gaussian fitting for the amplitude histogram, an average noise level ($\mu_{noise}$) of 0.18 pm and a noise deviation ($\sigma_{noise}$) of 0.1 pm were obtained as shown in Fig. 4c. Thus, in the absence of $V_{ac}$ excitation, the steady noise level can
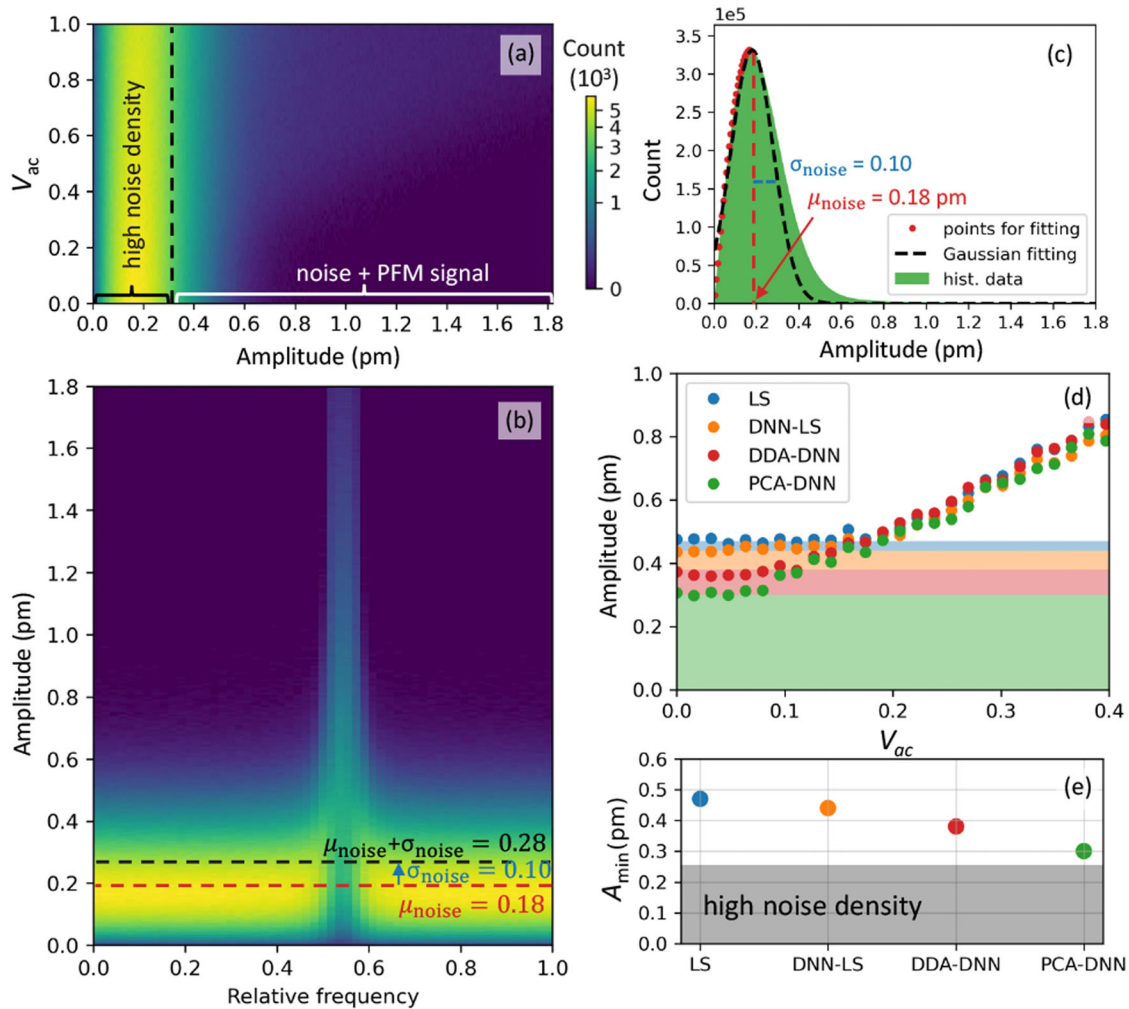
**Fig. 4  As-acquired signal of the PPLN dataset from the $V_{ac}$ amplitude sweep measurement. a** Amplitude spectral density as a function of $V_{ac}$, (**b**) amplitude spectral density as a function of a relative frequency, and (**c**) amplitude histogram with a Gaussian fit to obtain the steady noise floor. The Gaussian fit was performed on the half lower part, indicated by the red dotted line, to avoid fitting on the PFM signal. **d** The averaged fitted amplitude as a function of $V_{ac}$. The highlighted level is the baseline of which the amplitude value is constant. The minimum detectable displacement $A_{min}$, which is the baseline extracted from (**d**), is plotted in (**e**). The shadow highlight in (**e**) indicates the high noise density area.

be calculated from the sum of $\mu_{noise}$ and $\sigma_{noise}$ as 0.28 pm. Further, if the PFM amplitude is higher than $\sigma_{noise}$ under the $V_{ac}$ excitation, the PFM amplitude can be distinguished from the noise level, indicating that the PFM amplitude higher than 0.28 pm is possible to be extracted depending on the sensitivity of the SHO fitting and prediction workflow. In this context, we define the SNR as $A/\sigma_{noise}$ where $A$ is the PFM amplitude.

Then, we define sensitivity as a minimum detectable displacement, i.e., minimum PFM amplitude ($A_{min}$). The fitted and predicted amplitude values of the PPLN dataset were extracted from the single-phase area indicated by the red box in Fig. 3d and plotted in Fig. 4d. When the $V_{ac}$ amplitude is decreased, the fitted and predicted amplitude values are linearly decreased and then limited at the baseline[30], indicating the $A_{min}$ values fitted and predicted by different workflows. Accordingly, each baseline in Fig. 4d was fitted to extract the $A_{min}$ of each SHO fitting or predicting workflow. As a result, we obtained the sensitivity for LS, DNN-LS, DDA-DNN, and PCA-DNN as 0.48, 0.45, 0.38, and 0.30 pm, respectively. Furthermore, we calculated the minimum SNR (as $A_{min}/\sigma_{noise}$) for the different workflows, which are 4.8, 4.5, 3.8, and 3.0 for LS, DNN-LS, DDA-DNN, and PCA-DNN, respectively.

## Application of different workflows to the weak piezoresponse of ultra-thin ferroelectrics

To test hybrid workflows based on the denoising process, we measured the PFM hysteresis loops on the 10-nm-thick HZO thin film[31], and applied different methods to the results. Because the SNR of the PFM signal is highly related to the $V_{ac}$, we compared SHO fitting and prediction by the LS, DDA-DNN, and PCA-DNN methods on the PFM hysteresis loops with different $V_{ac}$, as shown in Fig. 5. At a low $V_{ac}$, the prediction of the DDA/PCA-DNN yielded a clear loop opening when compared to that of the traditional LS at a low $V_{ac}$, which gave an unclear hysteresis loop opening. The loop opening of PCA-DNN was relatively clearer compared to DDA-DNN at a low $V_{ac}$, allowing clear observation of the switching events of the HZO thin films.

The actual measurement using low $V_{ac}$ resulted in a different SNR in the acquired signal. The unclear hysteresis loop opening of the LS method (Fig. 5b, c) indicates the poor sensitivity of PFM hysteresis measurement[32], suggesting an inability of the LS method to extract the piezoresponse buried in the noise for SHO fitting. We examined the improvement of PFM hysteresis measurement through the deviation of the PFM hysteresis loop, as shown in Fig. 5d. The deviation of LS fitting was relatively higher
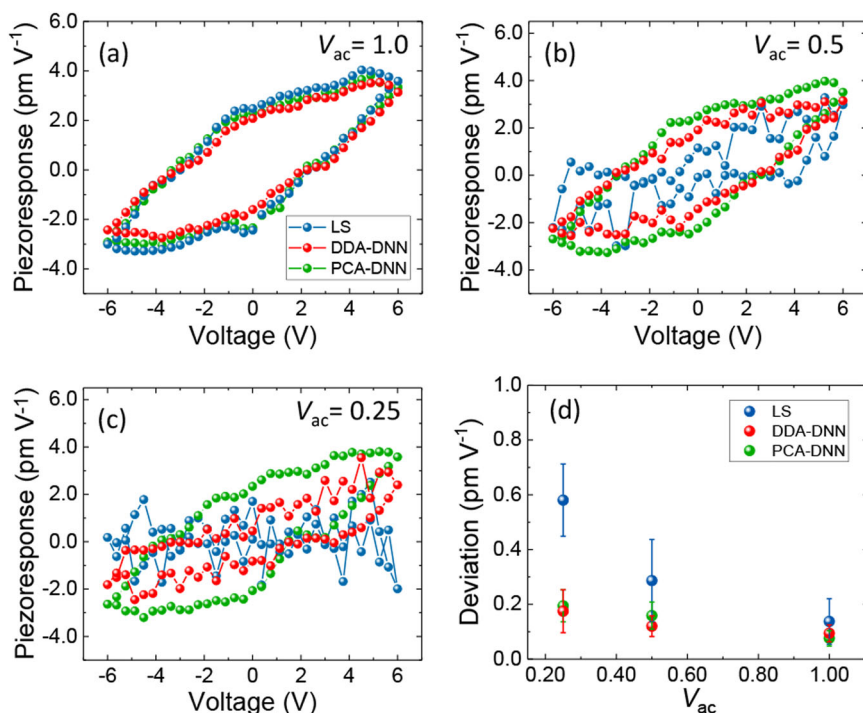
**Fig. 5 PFM hysteresis loops in HZO thin film.** The PFM was averaged from 3×3 mapping over an area of $1 \times 1 \, \mu m^2$ with SHO fitting and prediction using (**a**) 1.0 $V_{ac}$, (**b**) 0.5 $V_{ac}$, and (**c**) 0.25 $V_{ac}$, respectively. The PFM hysteresis loops were extracted using the (blue) LS, (red) DDA-DNN, and (green) PCA-DNN methods, respectively. All measured PFM piezoresponses were normalized by $V_{ac}$. **d** Deviation of an averaged PFM hysteresis loop corresponding to the SHO fitting and prediction methods.

than those of DDA-DNN and PCA-DNN, in which the DDA/PCA-DNN were remarkably improved in the sensitivity of the PFM hysteresis measurement at the low SNR. This improved PFM sensitivity using the hybrid workflow allowed measurements at a low $V_{ac}$ to avoid undesired responses caused by high voltage and facilitated the measurement on materials with weak piezoelectricity. We noted that, although DDA demonstrated a slightly inferior denoising result than that of PCA, it could be further improved with a neural architecture. Furthermore, if a noise signal is one of the primary components, e.g., 60 Hz noise, PCA may not properly work, and in this case, DDA may be more suitable.

In conclusion, in this study, we developed the hybrid prediction methods of DDA/PCA-DNN for SHO parameter extraction to address the poor fitting problem caused by data outliers in both standard LS and DNN-LS fitting. Furthermore, we obtained a satisfactory prediction comparison on the actual experimental $V_{ac}$ amplitude sweep dataset of PPLN, in which the SNR of the SHO parameter extraction was improved. Specifically, compared to the LS method with an SNR of 4.8 and sensitivity of 0.48 pm, the SNR has improved to 3.0 with a sensitivity of 0.30 pm for the PCA-DNN. We also demonstrated that the hybrid workflow can be applied to the PFM hysteresis loops in the HZO thin film. The hybrid methods improved the sensitivity of PFM hysteresis loops compared to the traditional LS fitting under a low SNR scenario because of the sample's weak piezoelectricity. Essentially, we pushed the fundamental limits of SNR and improved the sensitivity of the instruments using machine learning without any hardware modification for the PFM.

Because of its improved sensitivity, our hybrid approaches could provide more chances to explore the low piezoresponse of the ultra-thin ferroelectrics[14] and may be useful for measurements in challenging environments, such as in liquid settings[15,16], where the PFM measurements may result in a low response and a high noise floor. In addition, we see feasibility in the rapid work of DDA/PCA-DNN that could be helpful for the real-time analysis of

piezoresponse[33]. We also anticipate that deep learning-based functional fitting or prediction will improve the sensitivity of measurements in other AFM techniques, in which cantilever resonance is used as an operational mechanism, including non-contact AFM and BE-based techniques[34,35], or even resonance-based sensors, e.g., acoustic sensors. Furthermore, the idea of a denoising neuron network hybrid with deep learning can be helpful for other microscopic techniques, e.g., transition electron microscopy[36], as well.

## METHODS

PFM measurements A commercial AFM (NX-10, Park Systems) with Cr/Pt-coated conductive tips (Multi75E-G, BudgetSensors, nominal spring constant $k \approx 3 \, N \, m^{-1}$) was used for the AFM measurements. The PFM measurements were performed using the AFM with a function generator and data acquisition system (NI-PXIe 5122/5412, National Instruments) with LabVIEW/MATLAB-based BE measurements. The central frequency, bandwidth, and frequency bins of the BE waveform were 375 kHz, 80 kHz, and 56, respectively.

Materials The 10-nm-thick HZO thin film was deposited on highly doped p-type silicon by atomic layere deposition, and the PPLN was purchased from Asylum Research.

Neural network implementation Data processing was done using Python 3.8. The DNN, DDA, and PCA (TensorFlow) were built and trained using Keras with a TensorFlow backend. For the computations, an AMD Ryzen 9 5900 × 12-Core processor with a 3.70 GHz CPU and 64 GB of RAM was used along with an NVIDIA GeForce RTX 3080 Ti GPU with 12 GB of GDDR6 memory.

## DATA AVAILABILITY

The data that support the findings of this study are available from the corresponding author upon reasonable request.

## CODE AVAILABILITY
Python scripts used for the analysis are available from the authors upon request.

## REFERENCES
1. Boescke, T. S., Muller, J., Brauhaus, D., Schroder, U. & Bottger, U. Ferroelectricity in hafnium oxide thin films. *Appl. Phys. Lett.* **99**, 102903 (2011).
2. Schroeder, U., Park, M. H., Mikolajick, T. & Hwang, C. S. The fundamentals and applications of ferroelectric HfO2. *Nat. Rev. Mater.* **7**, 653–669 (2022).
3. Qiao, H., Wang, C., Choi, W. S., Park, M. H. & Kim, Y. Ultra-thin ferroelectrics. *Mater. Sci. Eng. R. Rep.* **145**, 10622 (2021).
4. Wang, C., Qiao, H. & Kim, Y. Perspective on the switching behavior of HfO2-based ferroelectrics. *J. Appl. Phys.* **129**, 010902 (2021).
5. Cheema, S. S. et al. Emergent ferroelectricity in subnanometer binary oxide films on silicon. *Science* **376**, 648–652 (2022).
6. Kwon, O., Seol, D., Qiao, H. & Kim, Y. Recent Progress in the Nanoscale Evaluation of Piezoelectric and Ferroelectric Properties via Scanning Probe Microscopy. *Adv. Sci.* **7**, 1901319 (2020).
7. Cheema, S. S. et al. Enhanced ferroelectricity in ultrathin films grown directly on silicon. *Nature* **580**, 478–482 (2020).
8. Kang, S. et al. Highly enhanced ferroelectricity in HfO2-based ferroelectric thin film by light ion bombardment. *Science* **376**, 731–738 (2022).
9. Yun, Y. et al. Intrinsic ferroelectricity in Y-doped HfO2 thin films. *Nat. Mater.* **21**, 903–909 (2022).
10. Zhang, Q. et al. Nanoscale Bubble Domains and Topological Transitions in Ultrathin Ferroelectric Films. *Adv. Mater.* **29**, 1702375 (2017).
11. Jesse, S. & Kalinin, S. V. Band excitation in scanning probe microscopy: sines of change. *J. Phys. D. Appl. Phys.* **44**, 464006 (2011).
12. Borodinov, N. et al. Deep neural networks for understanding noisy data applied to physical property extraction in scanning probe microscopy. *Npj Comput. Mater.* **5**, 1–8 (2019).
13. Kwon, O. et al. Quantitative Local Probing of Polarization with Application on HfO2-Based Thin Films. *Small Methods* **5**, 2100781 (2021).
14. Muller, J. et al. Ferroelectricity in Simple Binary ZrO$_2$ and HfO$_2$. *Nano Lett.* **12**, 4318–4323 (2012).
15. Balke, N., Jesse, S., Chu, Y. H. & Kalinin, S. V. High-Frequency Electromechanical Imaging of Ferroelectrics in a Liquid Environment. *ACS Nano* **6**, 5559–5565 (2012).
16. Carrasco, C., Ares, P., de Pablo, P. J. & Gomez-Herrero, J. Cutting down the forest of peaks in acoustic dynamic atomic force microscopy in liquid. *Rev. Sci. Instrum.* **79**, 126106 (2008).
17. Budil, D. E., Lee, S., Saxena, S. & Freed, J. H. Nonlinear-least-squares analysis of slow-motion EPR spectra in one and two dimensions using a modified Levenberg-Marquardt algorithm. *J. magn. reson., Ser. A* **120**, 155–189 (1996).
18. Denning, D., Guyonnet, J. & Rodriguez, B. J. Applications of piezoresponse force microscopy in materials research: from inorganic ferroelectrics to biopiezo-electrics and beyond. *Int. Mater. Rev.* **61**, 46–70 (2016).
19. Alikin, D. et al. Exploring Charged Defects in Ferroelectrics by the Switching Spectroscopy Piezoresponse Force Microscopy. *Small Methods* **6**, 2101289 (2022).
20. Hsain, H. A. et al. Enhanced piezoelectricity of thin film hafnia-zirconia (HZO) by inorganic flexible substrates. *Appl. Phys. Lett.* **113**, 022905 (2018).
21. Sriboriboon, P., Qiao, H., Kang, S., Sun, C. & Kim, Y. Ionically Mediated Mechanical Deformation Associated with Memristive Switching. *Adv. Funct. Mater.* **31**, 2103145 (2021).
22. Agar, J. C. et al. Revealing ferroelectric switching character using deep recurrent neural networks. *Nat. Commun.* **10**, 1–11 (2019).
23. Liu, Y., Yu, B. X., Liu, Z. W., Beck, D. & Zeng, K. Y. High-Speed Piezoresponse Force Microscopy and Machine Learning Approaches for Dynamic Domain Growth in Ferroelectric Materials. *ACS Appl. Mater. Interfaces* **12**, 9944–9952 (2020).
24. Liu, Y. T. et al. Experimental discovery of structure-property relationships in fer-roelectric materials via active learning. *Nat. Mach. Intell.* **4**, 341–350 (2022).
25. Hinton, G. E. & Salakhutdinov, R. R. Reducing the dimensionality of data with neural networks. *Science* **313**, 504–507 (2006).
26. Schmidt, J., Marques, M. R. G., Botti, S. & Marques, M. A. L. Recent advances and applications of machine learning in solid-state materials science. *Npj Comput. Mater.* **5**, 1–36 (2019).
27. Vogelstein, J. T. et al. Supervised dimensionality reduction for big data. *Nat. Commun.* **12**, 1–9 (2021).
28. Huang, B. Y., Esfahani, E. N. & Li, J. Y. Mapping intrinsic electromechanical responses at the nanoscale via sequential excitation scanning probe microscopy empowered by deep data. *Natl Sci. Rev.* **6**, 55–63 (2019).
29. Zhang, F. Y. et al. Maximizing Information: A Machine Learning Approach for Analysis of Complex Nanoscale Electromechanical Behavior in Defect-Rich PZT Films. *Small Methods* **5**, 2100552 (2021).
30. Seol, D., Kang, S., Sun, C. & Kim, Y. Significance of electrostatic interactions due to surface potential in piezoresponse force microscopy. *Ultramicroscopy* **207**, 112839 (2019).
31. Jesse, S., Baddorf, A. P. & Kalinin, S. V. Switching spectroscopy piezoresponse force microscopy of ferroelectric materials. *Appl. Phys. Lett.* **88**, 062908 (2006).
32. Xie, S. H. et al. High resolution quantitative piezoresponse force microscopy of BiFeO3 nanofibers with dramatically enhanced sensitivity. *Nanoscale* **4**, 408–413 (2012).
33. Liu, Y. T., Kelley, K. P., Funakubo, H., Kalinin, S. V. & Ziatdinov, M. Exploring Physics of Ferroelectric Domain Walls in Real Time: Deep Learning Enabled Scanning Probe Microscopy. *Adv. Sci.* **9**, 2203957 (2022).
34. Nikiforov, M. P. et al. Probing the temperature dependence of the mechanical properties of polymers at the nanoscale with band excitation thermal scanning probe microscopy. *Nanotechnology* **20**, 395709 (2009).
35. Collins, L. et al. Band excitation Kelvin probe force microscopy utilizing photo-thermal excitation. *Appl. Phys. Lett.* **106**, 104102 (2015).
36. Yang, S. H. et al. Deep Learning-Assisted Quantification of Atomic Dopants and Defects in 2D Materials. *Adv. Sci.* **8**, 2101099 (2021).

## AUTHOR CONTRIBUTIONS
Y.K. conceived the original idea and directed this work. P.S. conducted the computational and measurements with the help of O.K. P.S., H.Q., and Y.K. analyzed the dataset. R.V. and S.J. contribute to the Python code. All authors discussed the results and contributed to the paper.

## COMPETING INTERESTS
The authors declare no competing interests.

## ADDITIONAL INFORMATION
**Supplementary information** The online version contains supplementary material available at https://doi.org/10.1038/s41524-023-00982-0.

**Correspondence** and requests for materials should be addressed to Yunseok Kim.

**Reprints and permission information** is available at http://www.nature.com/reprints

**Publisher's note** Springer Nature remains neutral with regard to jurisdictional claims in published maps and institutional affiliations.